

Weyl points and Fermi arcs in a chiral phononic crystal

Feng Li^{1†}, Xueqin Huang^{1†}, Jiuyang Lu¹, Jiahong Ma¹ and Zhengyou Liu^{2,3*}

Topological semimetals are materials whose band structure contains touching points that are topologically nontrivial and can host quasiparticle excitations that behave as Dirac or Weyl fermions^{1–7}. These so-called Weyl points not only exist in electronic systems, but can also be found in artificial periodic structures with classical waves, such as electromagnetic waves in photonic crystals^{8–11} and acoustic waves in phononic crystals^{12,13}. Due to the lack of spin and a difficulty in breaking time-reversal symmetry for sound, however, topological acoustic materials cannot be achieved in the same way as electronic or optical systems. And despite many theoretical predictions^{12,13}, experimentally realizing Weyl points in phononic crystals remains challenging. Here, we experimentally realize Weyl points in a chiral phononic crystal system, and demonstrate surface states associated with the Weyl points that are topological in nature, and can host modes that propagate only in one direction. As with their photonic counterparts, chiral phononic crystals bring topological physics to the macroscopic scale.

Recently, interest in Weyl semimetals has been growing^{1–7}. Weyl semimetals are materials in which the electrons have linear dispersions in all directions while being doubly degenerate at a single point, called the Weyl point, near the Fermi surface in three-dimensional (3D) momentum space. In other words, the electrons in Weyl semimetals obey the Weyl equation and thus behave like Weyl fermions. The Weyl point is a source or sink of the Berry curvature flux in momentum space; in other words, it is a magnetic monopole with a topological charge, defined as the Berry curvature flux threading a sphere enclosing the Weyl point with a value of either +1 or –1, corresponding to the chirality of the Weyl fermion. The Weyl point and the associated topological invariants enable Weyl semimetals to exhibit a variety of unusual properties, including robust surface waves (SWs)^{14–16} and chiral anomaly^{17,18}. In addition to the standard Weyl points possessing a point-like Fermi surface (referred to as type-I), another type of Weyl point was more recently recognized, which has a conical Fermi surface (referred to as type-II)^{13,19–21}.

Since the Weyl point or Weyl cone in Weyl semimetals represents a special dispersion of electrons moving in periodic potentials, the question naturally arises as to whether a similar dispersion or the Weyl point for classical waves propagating in artificial periodic structures exists^{8–13,22–28}. Lu *et al.* were the first to report the existence of Weyl points and the associated one-way SWs in photonic crystals based on double-gyroid structures^{8,9}. Weyl points were also observed in photonic crystals fabricated using conventional planar fabrication technology^{10,11}. Following the developments of the Weyl photonic crystals, Weyl phononic crystals (PCs) with Weyl points

for acoustic waves have also been proposed in graphene-based structures with coupled cavities or coupled plane waveguides¹². More recently, Yang *et al.* proposed a scheme to obtain a Weyl PC by stacking dimerized chains in three dimensions, obtaining type-II Weyl points¹³. To date, the search for Weyl points in PCs has been a theoretical effort, and the realization of Weyl PCs in practice is therefore necessary.

In this work, we report the experimental observation of Weyl points in a 3D chiral PC¹². Since the time-reversal symmetry is preserved in the design, the Weyl points arise from the breaking of the inversion symmetry. Weyl points in the first Brillouin zone (BZ) are determined by measuring and Fourier transforming the field distributions of the bulk waves; the Fermi-arc dispersions of the SWs are similarly obtained by measuring and Fourier transforming the surface acoustic fields. The topologically protected one-way propagations of the SWs and their immunity to defects are all demonstrated experimentally. All observations are in agreement with the theoretical predictions.

The Weyl PC is fabricated based on a layer-stacking strategy: if a single layer can support two-dimensional (2D) linear dispersions with touching points, one can obtain Weyl points by stacking it layer by layer into a 3D structure with proper interlayer coupling. Figure 1a provides a photo of our sample, showing the stacked structured plates fabricated by 3D printing. Portions of the front and back surfaces of the structured plate together with a schematic of the outlined unit cells are shown in Fig. 1b,c, respectively. The unit cell on the front surface appears to be a protruding pillar surrounded by six holes symmetrically distributed through the plate in a spiral pattern. The unit cell has the side length $a = 7.0$ mm, and the central pillar has a radius $r_0 = 2.6$ mm and height $h = 6.1$ mm. For the holes, the radial dimension is determined from the difference between the radii $r_1 = 2.9$ mm and $r_2 = 5.5$ mm, and the angular dimension is determined by the separation $d = 1$ mm between two neighbouring holes. Across the plate (which has a thickness $L = 4.4$ mm), all holes twist at an angle of 90° in a spiral manner, such that the unit cell on the back surface appears as shown in Fig. 1c. Therefore, the unit cell has a total height $c = h + L = 10.5$ mm along the z direction. When the structured plates are stacked along the normal or z direction, two successive plates with a space between them form an in-plane waveguide. Two neighbouring waveguides are then coupled via the spiral holes through the separating plate. Therefore, the fabricated PC should be viewed, more accurately, as a stack of planar hollow waveguides, connected or coupled with spiral hollow channels. The hollow waveguides and channels are all filled with air, and we deal with the acoustic waves, namely the pressure waves propagating in air. Each in-plane waveguide supports 2D linear dispersions for the two lowest-order acoustic modes with touching points at the corners

¹School of Physics and Optoelectronic Technology, South China University of Technology, Guangzhou, Guangdong 510640, China. ²Key Laboratory of Artificial Micro- and Nanostructures of Ministry of Education and School of Physics and Technology, Wuhan University, Wuhan 430072, China. ³Institute for Advanced Studies, Wuhan University, Wuhan 430072, China. [†]These authors contributed equally to this work. *e-mail: zyliu@whu.edu.cn

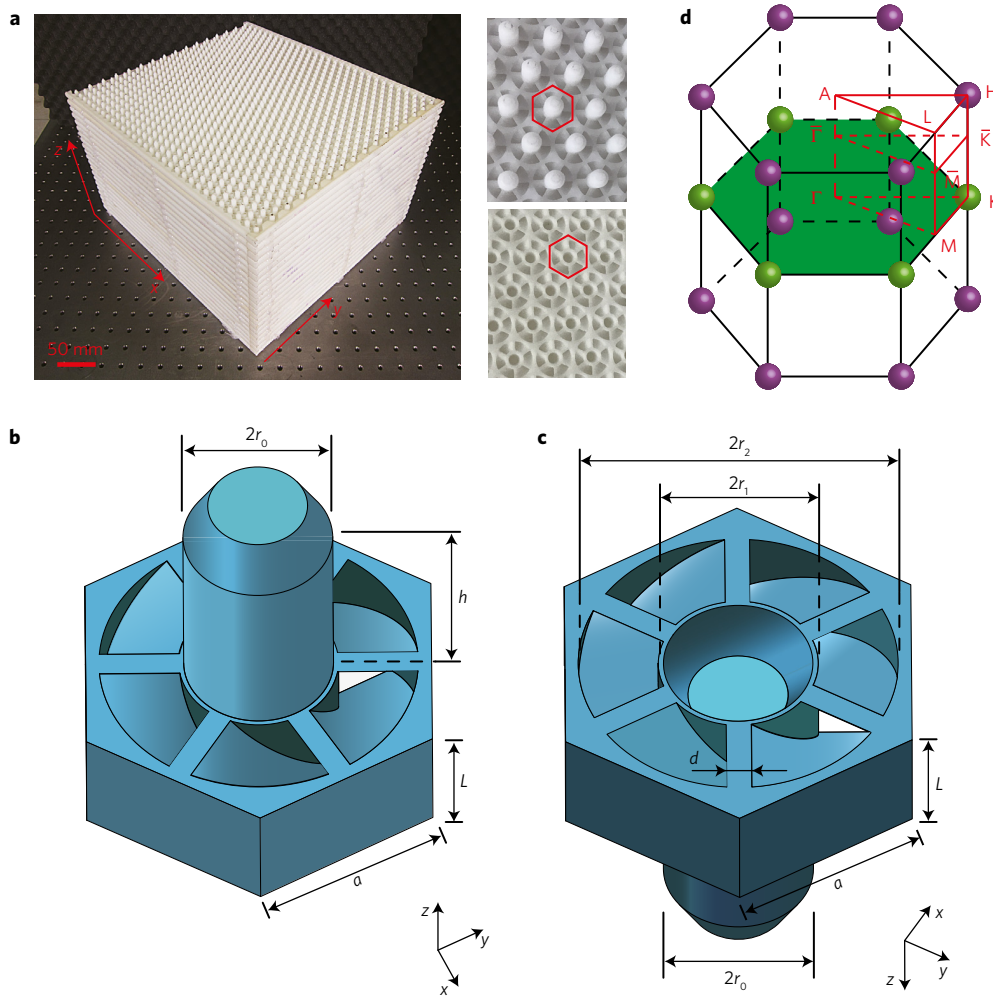


Figure 1 | Illustration of the unit cell of the phononic crystal. **a**, A photo of the 3D sample showing the stacking of the structured plates, together with magnified images of the front and back sides of one plate. **b, c**, The front and back views of the unit cell of the PC. **d**, The first Brillouin zone of the system. The purple and green spheres represent Weyl points with opposite topological charges, respectively.

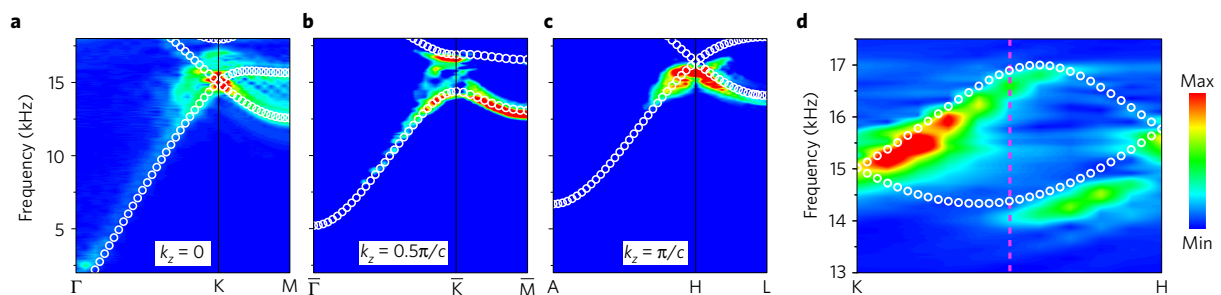


Figure 2 | Bulk bands of the two lowest modes. **a–d**, In planes $k_z = 0$ (**a**), $k_z = 0.5\pi/c$ (**b**), $k_z = \pi/c$ (**c**), and along the KH direction (**d**). The coloured maps represent the experimental data, while white circles represent the simulation results. The vertical dashed line in **d** marks $k_z = 0.5\pi/c$ for comparison with **b**.

of the 2D first BZ. When they are stacked along the z direction and connected with the spiral channels, the Weyl points can be expected in the 3D structure. The sample has a total height of 21 layers along the z direction and dimensions of 31 and 30 unit cells in the x and y directions, respectively. The hexagonal first BZ of the sample is shown in Fig. 1d.

Theoretical studies have shown that there are two pairs of Weyl points for the structure distributed on the $k_z = 0$ and $k_z = \pi/c$ planes in the first BZ, as shown in Fig. 1d. To confirm the existence of the Weyl points on the two planes, we measure the 2D band structures by fixing $k_z = 0$ and $k_z = \pi/c$. Figure 2a (2c) shows the measured

and calculated 2D band structures on the $k_z = 0$ ($k_z = \pi/c$) plane along the ΓK and KM (AH and HL) directions in the first BZ for the two lowest-order acoustic modes. The colour maps represent the experimental dispersions obtained by Fourier transforming the measured pressure fields inside the sample (Methods), and the white circles denote the calculated values obtained from full wave simulations (Methods). Double degeneracy and linear dispersions at the K (H) point are clearly observed at approximately 15.0 kHz (16.0 kHz) in Fig. 2a (2c) on plane $k_z = 0$ ($k_z = \pi/c$). However, a gap of approximately 2.0 kHz opens at the \bar{K} point on the plane $k_z = 0.5\pi/c$, the halfway point between $k_z = 0$ and $k_z = \pi/c$, as

shown in Fig. 2b, which can be attributed to the breaking of the time-reversal symmetry due to the effective gauge flux arising from the nonzero k_z . In all cases, the experimental results are in agreement with the numerical simulations.

To corroborate that the aforementioned K and H points are Weyl points, the dispersion should be measured along an additional direction, for example, the KH direction. The experimental and simulated results are shown together in Fig. 2d. The double degeneracies and linear dispersions of the two lowest modes at the K and H points are again exhibited. From the K to H points, the two bands evolve linearly then nonlinearly with the maximal bandgap in the middle of KH, and then linearly again when approaching the H point. Overall, the measurements are in agreement with the numerical simulations. The double degeneracies and the linear dispersions are checked along three independent directions, demonstrating that the K and H points are definitely Weyl points. Since C_6 symmetry is present in the system, the K' (H') point is also a Weyl point, and K' (H') possesses the same charge as K (H). However, neutrality requires that H (H') and K (K') have opposite charges. In addition, Weyl points H and H' have different frequencies than K and K' , which means that at the frequency of the Weyl point K or K' (H or H'), while there is a point-like equi-frequency surface at K or K' (H or H'), a closed (nearly spherical) equi-frequency surface surrounds the Weyl point H or H' (K or K'). Since there is no symmetry to relate K or K' to H or H' , the Weyl points with opposite charges are at different frequencies^{9,12}. In other words, no truly point-like equi-frequency surface exists in the Weyl PC.

One important feature of Weyl semimetals, Weyl photonic crystals, or Weyl PCs is the existence of robust topological one-way SWs on the sample surface. ‘One-way’ means that the SWs cannot be backscattered. This property may lead to possible applications of Weyl PCs in innovative acoustic devices. In contrast to the conventional surface acoustic waves that have closed equi-frequency dispersion curves, the SWs on the Weyl PCs form the so-called Fermi arc, which connect the projections of two oppositely charged Weyl points on the surface.

Note that the edge states can exist only on the XZ or the YZ surfaces and cannot exist on the XY surface because, on the XY surface, the projections of K and H coincide, and their charges cancel. To map out the Fermi arc on the XZ or YZ surface, we place a point source close to the centre of the XZ or YZ surface of the sample, which ensures the excitations of the surface states along all directions on the surface. Figure 3a shows the excited field on the XZ surface of the sample, and the inset shows a schematic of the sample, with the corresponding surface marked with a red star representing the excitation source. The point source has a frequency of 15.4 kHz. As observed in Fig. 3a, the SWs on the XZ surface clearly exhibit two branches: the up- and left-ward propagation branch and the down- and right-ward propagation branch, which are related by time-reversal symmetry. Similarly, we measure the field on the YZ surface excited by a point source at the surface centre, as shown in Fig. 3b, and similar features are observed. The absence of the edge states on the XY surface can be confirmed by the similar experiment conducted on the XY surface, as given in the Supplementary Methods.

By Fourier transforming the measured fields, we can arrive at the dispersion surface of the surface states or the Fermi arcs at the working frequency. Figure 3c shows the Fermi arcs of the surface states on the XZ surface and projections of the bulk Weyl points H (H') and K (K') in the 2D momentum space of the XZ surface. The colour map shows the experimental results, and the white solid lines represent the calculated values. For comparison, we also show the calculated Fermi arcs of the surface states on the opposite XZ surface as white dashed lines. Vertical black lines mark the boundaries of the first BZ of the XZ surface. Clearly, the Fermi arc starts from the projection of K. However, it does not end at the projection of H but somewhere on

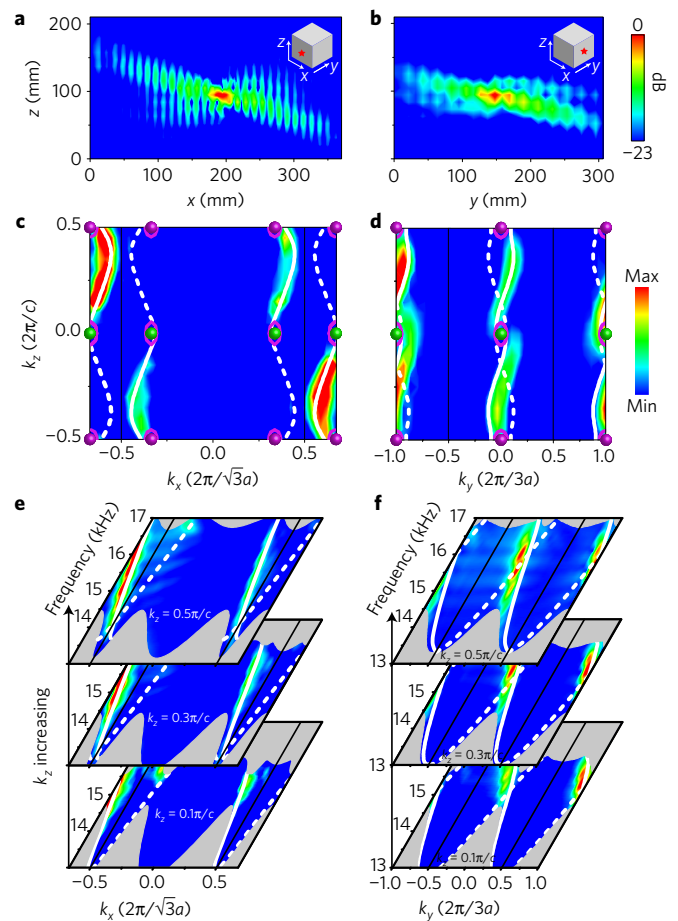


Figure 3 | Surface waves and the dispersions. **a, b**, The SW fields excited by point sources placed at the centre of the XZ and YZ surfaces, respectively. The insets show schematics of the sample, and red stars indicate the positions of excitation. **c, d**, Fourier transforms of the SW fields on the XZ and YZ surfaces, respectively, showing the contours of the Fermi arcs of the surface states at the frequency of 15.4 kHz. The white solid lines represent the corresponding simulated Fermi arcs, while the white dashed lines represent the Fermi arcs of the SWs on opposite surfaces. The green and purple spheres denote the Weyl points with opposite charges. The purple semicircles represent the equi-frequency contours of 15.4 kHz surrounding the Weyl point H or H' . **e, f**, The dispersion relations of the SWs with fixed $k_z = 0.1\pi/c$, $0.3\pi/c$ and $0.5\pi/c$ on XZ and YZ surfaces, respectively. The colour maps represent the experimental results obtained by Fourier transforming the fields excited by point sources. The white solid lines represent the simulated results. For a comparison, the dispersion relations of the SWs on the opposite surfaces obtained by simulations are given by the white dashed lines.

the equi-frequency surface (purple curves) of the working frequency around the projection of H because the Weyl points H and K have different frequencies, and at the working frequency—that is, the frequency of point K—a spherical equi-frequency surface surrounds the H point. Similarly, we show the measured and calculated Fermi arcs for the edge states on YZ surfaces in Fig. 3d. However, in this case, the projection of K coincides with that of K' , and the projection of H coincides with that of H' .

To obtain further insight into the SWs, we study the dispersion behaviours of the surface states along the x and y directions with fixed $k_z = 0.1\pi/c$, $0.3\pi/c$ and $0.5\pi/c$, as shown in Fig. 3e,f, respectively. The coloured regions show the gap ranging from 13 kHz to 17 kHz (see also Fig. 2b), while the white areas above and below show the bulk propagation bands. Again, the colour

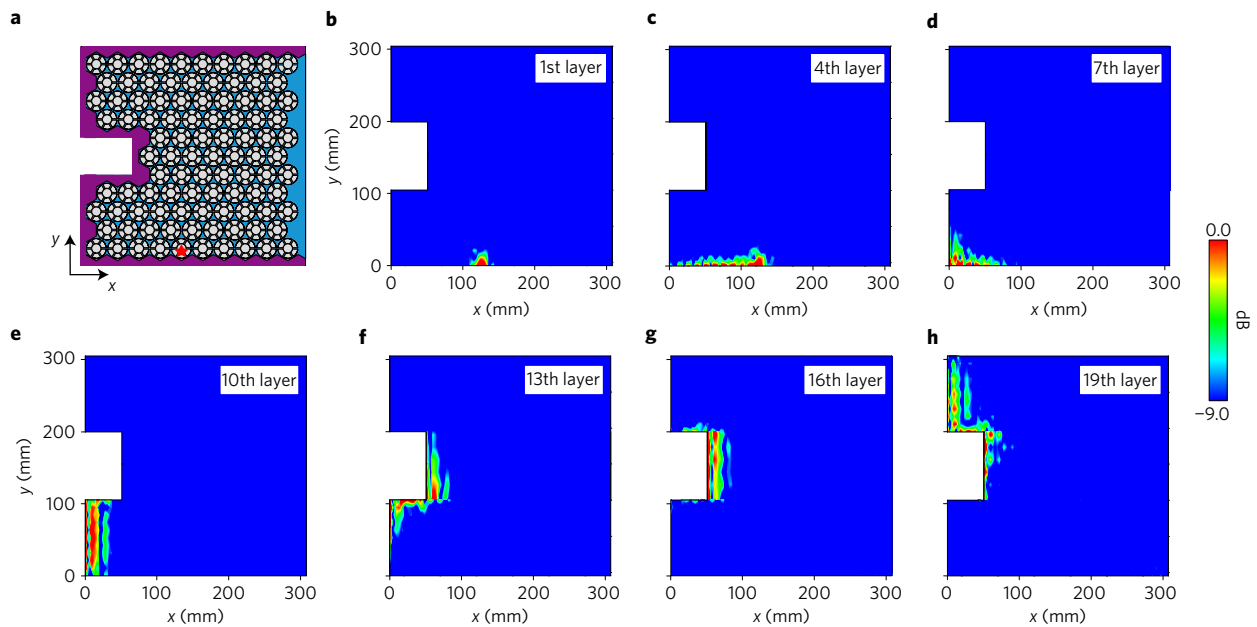


Figure 4 | Experimental one-way propagation of surface states in the presence of a defect. **a**, The schematic of a sample with a defect indented on the YZ surface. The sample is covered by a rigid material, as indicated by purple, on three surfaces (including two XZ surfaces and the YZ surface with the defect), which ensures the existences of the SWs on these surfaces. The red star labels the position of excitation. **b–h**, The field distributions of the SWs on the boundaries of seven layers, numbered 1, 4, 7, 10, 13, 16 and 19 of the sample. The SW propagates through the sample corners and the defect without backscattering. Here, to more clearly demonstrate the one-way propagation, the colour maps have been scaled up by 1.9 dB for every layer to compensate for absorption by air.

maps (within the bulk bandgap) represent the measured dispersion curves of the SWs, while the white solid curves represent the calculated curves. The dispersion curves of the surface states on the opposite surface (only calculated) are indicated by the white dashed curves. Evidently, all surface modes have the feature emerging from the lower propagation band to the upper propagation band. Figure 3c,e elucidates the branching field pattern on the XZ surface, excited by a point source, as shown in Fig. 3a. The surface states with $k_z > 0$ (for example, take $k_z = 0.5\pi/c$) and the group velocities pointing to the negative x direction, as shown in Fig. 3e, contribute to the up- and left-ward propagating branch. Their time-reversal-related counterparts give rise to the down- and right-ward propagating branch. The branching field pattern in Fig. 3b can be understood similarly.

The Fermi arcs in Fig. 3c,d demonstrate that the SWs with fixed k_z can propagate only along one direction on either the XZ or YZ surfaces. Such topologically protected one-way propagation is also robust and immune to defects. To demonstrate this robustness, we create an indented rectangular defect on the YZ surface of the sample, as shown in Fig. 4a. The set-up for measuring the propagation of SWs in the sample with the defect is provided schematically in Methods. To excite the SWs with $k_z = 0.5\pi/c$, four sequential point sources with identical frequencies of 15.4 kHz but phases increasing by $\pi/2$ are placed in the position indicated by a star in Fig. 4a from the first to the fourth layer of the sample. We scan the field inside the sample layer by inserting a probe into the space (that is, the plane waveguide) in each layer. Starting from the first layer, we pick up one layer from every three layers to show the field distribution inside, which gives a total of seven field distributions, as shown in Fig. 4b–h. This scan clearly demonstrates that the SW can propagate only in a clockwise manner along the boundary, and does not reflect or scatter due to the corners or the defect that it encounters. Note that SWs considerably attenuate during propagation due to the absorption in air; therefore, the colour maps in Fig. 4b–h have been scaled up by 1.9 dB per layer to better demonstrate this propagation.

The Weyl points for acoustic waves observed in our experiment open the door to 3D topological acoustics, in addition to the 2D topological acoustics, recently implemented in acoustic topological insulators and valley acoustics^{29–33}. Near the Weyl-point frequency, Weyl phononic crystals provide directional selectivity for filtering sound incident from any direction and enable the pseudo-diffusive transport of sound. The unique Berry curvature field associated with the Weyl points can lead to the weak localization of sound against disorder in Weyl acoustic materials. The topologically protected one-way surfaces may lead to potential applications of Weyl PCs in innovative acoustic devices.

Methods

Methods, including statements of data availability and any associated accession codes and references, are available in the [online version of this paper](#).

Received 22 May 2017; accepted 29 August 2017;
published online 2 October 2017

References

- Soluyanov, A. A. *et al.* Type-II Weyl semimetals. *Nature* **527**, 495–498 (2015).
- Xu, S.-Y. *et al.* Discovery of a Weyl fermion semimetal and topological Fermi arcs. *Science* **349**, 613–617 (2015).
- Lv, B. Q. *et al.* Experimental discovery of Weyl semimetal TaAs. *Phys. Rev. X* **5**, 031013 (2015).
- Xu, S. *et al.* Discovery of a Weyl fermion state with Fermi arcs in niobium arsenide. *Nat. Phys.* **11**, 748–754 (2015).
- Lv, B. Q. *et al.* Observation of Weyl nodes in TaAs. *Nat. Phys.* **11**, 724–727 (2015).
- Shekhar, C. *et al.* Extremely large magnetoresistance and ultrahigh mobility in the topological Weyl semimetal candidate NbP. *Nat. Phys.* **11**, 645–649 (2015).
- Yang, L. X. *et al.* Weyl semimetal phase in the non-centrosymmetric compound TaAs. *Nat. Phys.* **11**, 728–732 (2015).
- Lu, L., Fu, L., Joannopoulos, J. D. & Soljacic, M. Weyl points and line nodes in gyroid photonic crystals. *Nat. Photon.* **7**, 294–299 (2013).
- Lu, L. *et al.* Experimental observation of Weyl points. *Science* **349**, 622–624 (2015).

10. Chen, W. J., Xiao, M. & Chan, C. T. Photonic crystals possessing multiple Weyl points and the experimental observation of robust surface states. *Nat. Commun.* **7**, 13038 (2016).
11. Noh, J. *et al.* Experimental observation of optical Weyl points and Fermi arc-like surface states. *Nat. Phys.* **13**, 611–617 (2017).
12. Xiao, M. *et al.* Synthetic gauge flux and Weyl points in acoustic systems. *Nat. Phys.* **11**, 920–924 (2015).
13. Yang, Z. & Zhang, B. Acoustic type-II Weyl nodes from stacking dimerized chains. *Phys. Rev. Lett.* **117**, 224301 (2016).
14. Wan, X., Turner, A. M., Vishwanath, A. & Savrasov, S. Y. Topological semimetal and Fermi-arc surface states in the electronic structure of pyrochlore iridates. *Phys. Rev. B* **83**, 205101 (2011).
15. Burkov, A. A. & Balents, L. Weyl semimetal in a topological insulator multilayer. *Phys. Rev. Lett.* **107**, 127205 (2011).
16. Potter, A. C., Kimchi, I. & Vishwanath, A. Quantum oscillations from surface Fermi arcs in Weyl and Dirac semimetals. *Nat. Commun.* **5**, 5161 (2014).
17. Son, D. T. & Spivak, B. Z. Chiral anomaly and classical negative magnetoresistance of Weyl metals. *Phys. Rev. B* **88**, 104412 (2013).
18. Huang, X. *et al.* Observation of the chiral-anomaly-induced negative magnetoresistance in 3D Weyl semimetal TaAs. *Phys. Rev. X* **5**, 031023 (2015).
19. Deng, K. *et al.* Experimental observation of topological Fermi arcs in type-II Weyl semimetal MoTe₂. *Nat. Phys.* **12**, 1105–1110 (2016).
20. Xu, Y., Zhang, F. & Zhang, C. Structured Weyl points in spin-orbit coupled Fermionic superfluids. *Phys. Rev. Lett.* **115**, 265304 (2015).
21. Xu, Y. & Duan, L. M. Type-II Weyl points in three-dimensional cold-atom optical lattices. *Phys. Rev. A* **94**, 053619 (2016).
22. Wang, L., Jian, S.-K. & Yao, H. Topological photonic crystal with equifrequency Weyl points. *Phys. Rev. A* **93**, 061801(R) (2016).
23. Bravo-Abad, J. *et al.* Weyl points in photonic-crystal superlattices. *2D Mater.* **2**, 034013 (2015).
24. Gao, W. *et al.* Photonic Weyl degeneracies in magnetized plasma. *Nat. Commun.* **7**, 12435 (2016).
25. Xiao, M., Lin, Q. & Fan, S. Hyperbolic Weyl point in reciprocal chiral metamaterials. *Phys. Rev. Lett.* **117**, 057401 (2016).
26. Shastri, K., Yang, Z. & Zhang, B. Realizing type-II Weyl points in an optical lattice. *Phys. Rev. B* **95**, 014306 (2017).
27. Dubcek, T. *et al.* Weyl points in three-dimensional optical lattices: synthetic magnetic monopoles in momentum space. *Phys. Rev. Lett.* **114**, 225301 (2015).
28. Hou, J.-M. & Chen, W. Weyl semimetals in optical lattices: moving and merging of Weyl points, and hidden symmetry at Weyl points. *Sci. Rep.* **6**, 33512 (2016).
29. He, C. *et al.* Acoustic topological insulator and robust one-way sound transport. *Nat. Phys.* **12**, 1124–1129 (2016).
30. Lu, J. *et al.* Observation of topological valley transport of sound in sonic crystals. *Nat. Phys.* **13**, 369–374 (2016).
31. Yang, Z. *et al.* Topological acoustics. *Phys. Rev. Lett.* **114**, 114301 (2015).
32. Fleury, R., Khanikaev, A. B. & Alu, A. Floquet topological insulators for sound. *Nat. Commun.* **7**, 11744 (2016).
33. Susstrunk, R. & Huber, S. D. Observation of phononic helical edge states in a mechanical topological insulator. *Science* **349**, 47–50 (2015).

Acknowledgements

This work is supported by the National Basic Research Program of China (Grant No. 2015CB755500), the National Natural Science Foundation of China (Grant Nos 61271139, 11572318, 11604102, and 11374233), Guangdong Innovative and Entrepreneurial Research Team Program (Grant No. 2016ZT06C594) and the National Postdoctoral Program for Innovative Talents (BX201600054).

Author contributions

Z.L. initiated and supervised the project. F.L. designed and performed the experiments. X.Q.H. and J.Y.L. carried out the numerical simulations. Z.L., F.L., X.Q.H. and J.Y.L. wrote the manuscript. All authors contributed to the analyses and discussions of the manuscript.

Additional information

Supplementary information is available in the [online version of the paper](#). Reprints and permissions information is available online at www.nature.com/reprints. Publisher's note: Springer Nature remains neutral with regard to jurisdictional claims in published maps and institutional affiliations. Correspondence and requests for materials should be addressed to Z.L.

Competing financial interests

The authors declare no competing financial interests.

Methods

Numerical simulation approach. All simulations in this work are performed using the commercial COMSOL Multiphysics solver package. Because of the huge acoustic impedance contrast between the plastic stereolithography material and air, the plastic material can be considered a hard boundary during the simulations. The bulk band structures in Fig. 2 are calculated using one unit cell with periodic boundary conditions in all three directions. The dispersions of SWs are obtained using ribbon structures with periodic boundary conditions in the specified directions. Here, to calculate the dispersions of SWs in the XZ surface, the periodic boundary conditions are imposed in the x and z directions (Fig. 3c,e), while for the YZ surface, the periodic boundary conditions are in the y and z directions (Fig. 3d,f). In both cases, along the third direction, the periodicity after 15 periods is terminated by rigid boundaries on the corresponding surfaces. The systems are filled with air (density = 1.18 kg m^{-3} , speed of sound = 346 m s^{-1} at room temperature).

Experimental measurements. A sub-wavelength (diameter = 6.0 mm) headphone is used for sound excitation. It basically covers the wavevector range in need. For bulk or surface states excitations, the headphone is separately placed at the centre (point A in Supplementary Fig. 1) of the bottom (XY) surface or the centre of the corresponding surfaces (red marks in Supplementary Fig. 2) with rigid boundaries. For the measurement of acoustic fields, a sub-wavelength microphone probe (diameter = 4 mm) attached to the tip of a stainless-steel rod is inserted into the sample through the space between the plates (Supplementary Fig. 1). The probe is controlled by a stage moving in three directions. The steps of the stage are 2.0 mm, 10.5 mm and 10.5 mm in the x , y and z directions, respectively. Sound signals (S-parameter S21) are sent and recorded by a network analyser (Keysight 5061B). The bulk and SW dispersions of the acoustic system are obtained by Fourier transforming the measured fields.

Data availability. The data that support the plots within this paper and other findings of this study are available from the corresponding author upon reasonable request.